

LETTER TO THE EDITOR

# Extended high-ionization [Mg iv] emission tracing widespread shocks in starbursts seen by *JWST*/NIRSpec

Miguel Pereira-Santaella<sup>1</sup>, Ismael García-Bernete<sup>2</sup>, Eduardo González-Alfonso<sup>3</sup>, Almudena Alonso-Herrero<sup>4</sup>, Luis Colina<sup>5</sup>, Santiago García-Burillo<sup>6</sup>, Dimitra Rigopoulou<sup>2,7</sup>, Santiago Arribas<sup>5</sup>, and Michele Perna<sup>5</sup>

(Affiliations can be found after the references)

April 26, 2024

## ABSTRACT

We report the detection of extended ( $>0.5$ – $1$  kpc) high-ionization [Mg iv]  $4.487\ \mu\text{m}$  (80 eV) emission in four local luminous infrared galaxies observed with *JWST*/NIRSpec. Excluding the nucleus and outflow of the Type 1 active galactic nucleus (AGN) in the sample, we find that the [Mg iv] luminosity is well correlated with that of H recombination lines, which mainly trace star forming clumps in these objects, and that the [Ar vi]  $4.530\ \mu\text{m}$  (75 eV), usually seen in AGN, is undetected. On 100–400 pc scales, the [Mg iv] line profiles are broader ( $\sigma(\text{[Mg iv]}) = 90 \pm 25\ \text{km s}^{-1}$ ) and shifted ( $\Delta v$  up to  $\pm 50\ \text{km s}^{-1}$ ) compared to those of the H recombination lines and lower ionization transitions (e.g.,  $\sigma(\text{H}\alpha) = 57 \pm 15\ \text{km s}^{-1}$ ). The [Mg iv] kinematics follow the large scale rotating velocity field of these galaxies and the broad [Mg iv] profiles are compatible with the broad wings detected in the H recombination lines. Based on these observational results, extended highly ionized gas more turbulent than the ambient interstellar medium, possibly as a result of ionizing shocks associated with star-formation, is the most likely origin of the [Mg iv] emission. We also computed new grids of photoionization and shock models to investigate where the [Mg iv] line originates. Shocks with velocities of 100–130  $\text{km s}^{-1}$  reproduce the observed line ratios and the [Mg iv] luminosity agrees with that expected from the mechanical energy released by supernovae (SNe) in these regions. Therefore, these models support shocks induced by SNe as the origin of the [Mg iv] line. Future studies on the stellar feedback from SNe will benefit from the [Mg iv] line that is little affected by obscuration and, in absence of an AGN, can only be produced by shocks due to its high ionization potential.

**Key words.** Galaxies: active – Galaxies: evolution – Galaxies: starburst – Infrared: ISM

## 1. Introduction

Feedback from active galactic nuclei (AGN) is an important element for the evolution of galaxies (e.g., Weinberger et al. 2018). However, detecting deeply buried AGN is still difficult due to dust obscuration. This is particularly challenging in local luminous and ultra-luminous infrared (IR) galaxies (U/LIRGs;  $L_{\text{IR}} > 10^{11} L_{\odot}$ ). Local U/LIRGs are mostly interacting/merging systems, so they represent a key phase in the evolution of galaxies (e.g., Patton et al. 2020), and their activity (AGN and star-formation) occurs in extremely dust-embedded environments.

Activity diagnostics in the optical fail in many U/LIRGs since they host the most obscured nuclei in the local Universe ( $N_{\text{H}} > 10^{25}\ \text{cm}^{-2}$ ; e.g., Falstad et al. 2021; García-Bernete et al. 2022a). Indirect methods using mid-IR spectroscopy pointed out the presence of AGN in a large fraction,  $\sim 70\%$ , of ULIRGs (e.g., Nardini et al. 2009; Veilleux et al. 2009). These mid-IR methods suggested a modest AGN contribution to the total luminosity. However, radio and sub-mm observations, which are insensitive to dust extinction, revealed compact nuclei exceeding the surface brightness density of a maximal starburst, hence likely AGN, dominating the bolometric luminosity of the majority of ULIRGs (Barcos-Muñoz et al. 2017; Pereira-Santaella et al. 2021; Hayashi et al. 2021). Therefore, the direct detection of these AGN remains elusive and its exact contribution to the total luminosity is still debated.

The reduced dust extinction in the near- and mid-IR spectral ranges, along with the superb sensitivity and angular resolution of the James Webb Space Telescope (*JWST*), for the first time allows the search for high-ionization emission lines, which may

eventually provide direct evidence of these elusive AGN in U/LIRGs. Specifically, the [Mg iv]  $4.487\ \mu\text{m}$  line, with a high ionization potential (IP; 80 eV), is not expected in gas photoionized by young stars since they do not emit significant quantities of photons with the energies beyond 54 eV ( $\text{He}^+$  ionization energy). Therefore, the detection of the [Mg iv] line, which lies close to the minimum of the dust opacity (e.g., Corrales et al. 2016), has been proposed as an excellent tracer of deeply embedded AGN (e.g., Satyapal et al. 2021). However, fast ionizing shocks ( $>80\ \text{km s}^{-1}$ ; Sutherland & Dopita 2017) can also produce highly ionized gas that can emit high-ionization lines. For instance, the [O iv]  $25.9\ \mu\text{m}$  line (IP 55 eV), which is well correlated with the AGN power (e.g., Diamond-Stanic et al. 2009; Pereira-Santaella et al. 2010b; García-Bernete et al. 2016), is also associated with shocks in starbursts (e.g., Lutz et al. 1998; Petric et al. 2011; Alonso-Herrero et al. 2012).

In this Letter, we investigate the origin (AGN, star-formation, or shocks) of the extended [Mg iv] emission detected in a sample of four local LIRGs observed with the *JWST*/Near Infrared Spectrograph (NIRSpec; Jakobsen et al. 2022). We first analyze the spatial distribution of the [Mg iv] emission and compare the [Mg iv] line profiles with those of other low-ionization and H recombination lines. Then, we use new grids of photoionization and shock models to determine the physical and dynamical conditions of the gas producing this line.

## 2. Sample and data reduction

Four local ( $39 < D_L/\text{Mpc} < 161$ ) LIRGs, with  $L_{\text{IR}} = 10^{11.6-11.9} L_{\odot}$ , were observed with *JWST*/NIRSpec using the high spectral res-

arXiv:2404.16641v1 [astro-ph.GA] 25 Apr 2024

**Table 1.** Sample of local LIRGs

Object	$D_L^a$ (Mpc)	$\log L_{\text{IR}}/L_{\odot}^a$	Interaction stage <sup>b</sup>	AGN <sup>c</sup>
VV 114 E	85.5	11.71	c	Obs. ? (1,2)
NGC 3256 N*	38.9	11.64	d	No (3)
NGC 3256 S*				Obs. (4)
II Zw 096	161	11.94	c	Obs. ? (5)
NGC 7469	70.8	11.65	a	Type 1 (6)

**Notes.** <sup>(a)</sup> Luminosity distance and 8-1000  $\mu\text{m}$  IR luminosity from [Armus et al. \(2009\)](#). <sup>(b)</sup> Interaction stage (a=pre-merger, c=mid-stage merger, and d=late stage merger) from [Stierwalt et al. \(2013\)](#). <sup>(c)</sup> AGN classification (Obs. = dust obscured AGN based on indirect evidences). “?” indicates inconclusive AGN detections. <sup>(\*)</sup> The separation between the two nuclei of NGC 3256 is  $\sim 5''.2$ , thus their NIRSpect observations ( $\sim 0''.16$  angular resolution at 4.5  $\mu\text{m}$ ) are well spatially resolved.

**References.** (1) [Rich et al. 2023](#); (2) [Donnan et al. 2023](#); (3) [Pereira-Santaella et al. 2010a](#); (4) [Ohyama et al. 2015](#); (5) [Inami et al. 2022](#); (6) [Osterbrock & Martel 1993](#)

olution grating G395H ( $R \sim 1900\text{--}3600$ ;  $2.87\text{--}5.27 \mu\text{m}$ ) and the integral field unit (IFU) mode ([Böker et al. 2022](#)), and with *JWST*/Mid-Infrared Instrument (MIRI) using all the bands of the Medium Resolution Spectrograph (MRS; [Wright et al. 2023](#); [Argyriou et al. 2023](#)). These observations were part of the Director’s Discretionary Early Release Science (DD-ERS) Program #1328 (PI: L. Armus and A. Evans). These four objects cover a wide range of properties: from pre-mergers to late merger stages and from heavily obscured AGN to Type 1 AGN (see Table 1).

For the data reduction, we used the *JWST* calibration pipeline (version 1.12.4; [Bushouse et al. 2023](#)) and the context 1197. We followed the standard reduction recipe complemented by a number of custom steps to reduce the effect of bad pixels and cosmic rays. Further details on the data reduction of the NIRSpect and MIRI/MRS data observations be found in [Pereira-Santaella et al. \(2022, 2024\)](#) and [García-Bernete et al. \(2024a\)](#).

### 3. Analysis and results

#### 3.1. Spatially extended [Mg iv] emission

Fig. 1 shows the rest-frame 4.31–4.57  $\mu\text{m}$  spectra from 23 regions selected in the four systems. To extract these spectra we used apertures with a diameter of  $0''.54$  (100–400 pc depending on the target). We did not apply any aperture correction as the emission appears spatially resolved. Nevertheless, in a worst-case scenario of a point source, the error in the line ratios discussed below (Sect. 4) would be small,  $<5\%$ . The regions were selected to cover the extended [Mg iv] emission detected in the line maps (see Figs. 2 and A.1-A.4). For simplicity, in this Letter we excluded regions with strong CO  $\nu=1\text{--}0$  band, since the [Mg iv] transition is almost coincident with the CO  $\nu=1\text{--}0$  R(24) 4.489  $\mu\text{m}$  line (Fig. 1). We note, however, that after modeling the band, it is possible to detect [Mg iv] emission also in these regions (see [González-Alfonso et al. 2024](#); [García-Bernete et al. 2024b](#)).

The spectra show clear [Mg iv] detections, two  $\text{H}_2$  lines, the Humphreys-12 4.376  $\mu\text{m}$  (Hu-12) recombination line, and, in some cases, weak absorptions from the R-branch of the CO  $\nu=1\text{--}0$  band. The [Ar vi] 4.530  $\mu\text{m}$  transition, with an IP of 75 eV slightly lower than [Mg iv], is only detected in the nucleus and outflow of the Type 1 AGN NGC 7469 with both lines having comparable intensities (see also [Bianchin et al. 2023](#)). The lat-

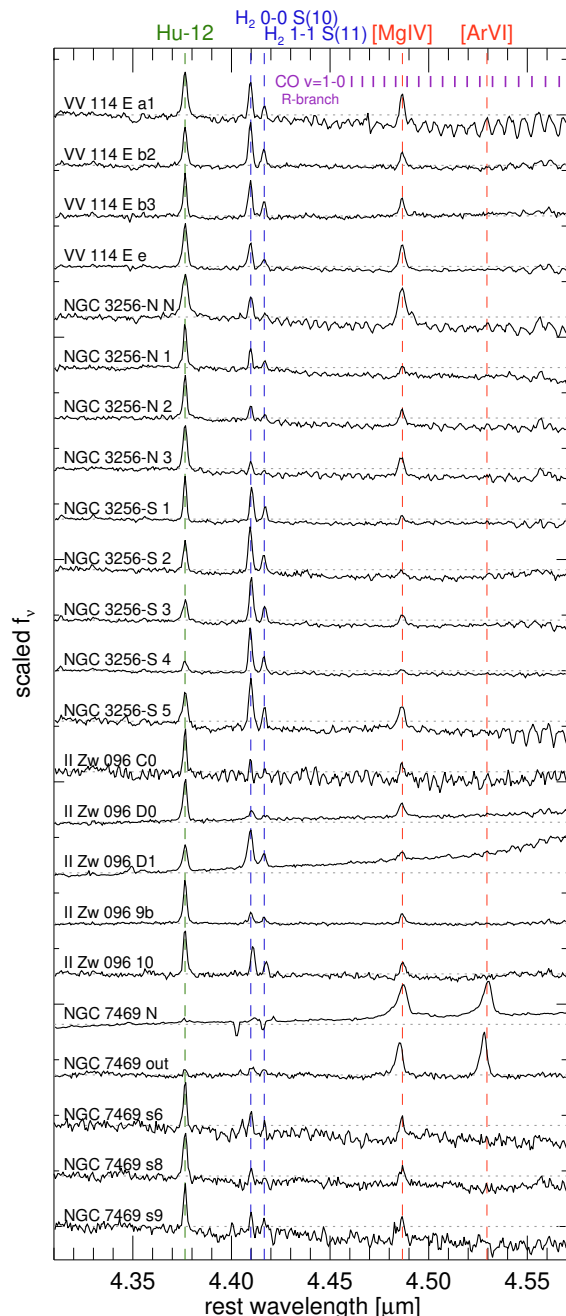


**Fig. 1.** Scaled and shifted *JWST*/NIRSpect 4.31–4.57  $\mu\text{m}$  spectra of the selected regions (see Sect. 3.1 and Figs. 2 and A.1-A.4). The wavelength of the transitions tracing ionized gas (Hu-12), warm molecular gas ( $\text{H}_2$  0–0 S(10) 4.410  $\mu\text{m}$  and 1–1 S(11) 4.417  $\mu\text{m}$ ), highly ionized gas ([Mg iv] and [Ar vi]), and the CO  $\nu=1\text{--}0$  band are indicated by the green, blue, red, and purple vertical lines, respectively.

ter is consistent with the *Infrared Space Observatory* (ISO) detections of the [Mg iv] and [Ar vi] line pair in two AGN (Circinus and NGC 1068), where the [Ar vi] line is  $\sim 2$  times brighter ([Sturm et al. 2002](#)). Based on these previous results for AGN, the absence of the [Ar vi] transition in the remaining regions is surprising and suggests that distinct physical conditions, maybe not related to an AGN, can lead to this [Mg iv] emission.

To determine the origin of the [Mg iv] line, we created 2D emission maps of tracers of the ionized gas phase (Hu-12 and Pf- $\gamma$  3.741  $\mu\text{m}$ ), the warm molecular gas phase ( $\text{H}_2$  0–0 S(8) 5.053  $\mu\text{m}$ ), and fast shocks ([Fe II] 5.340  $\mu\text{m}$ ). Warm molec-

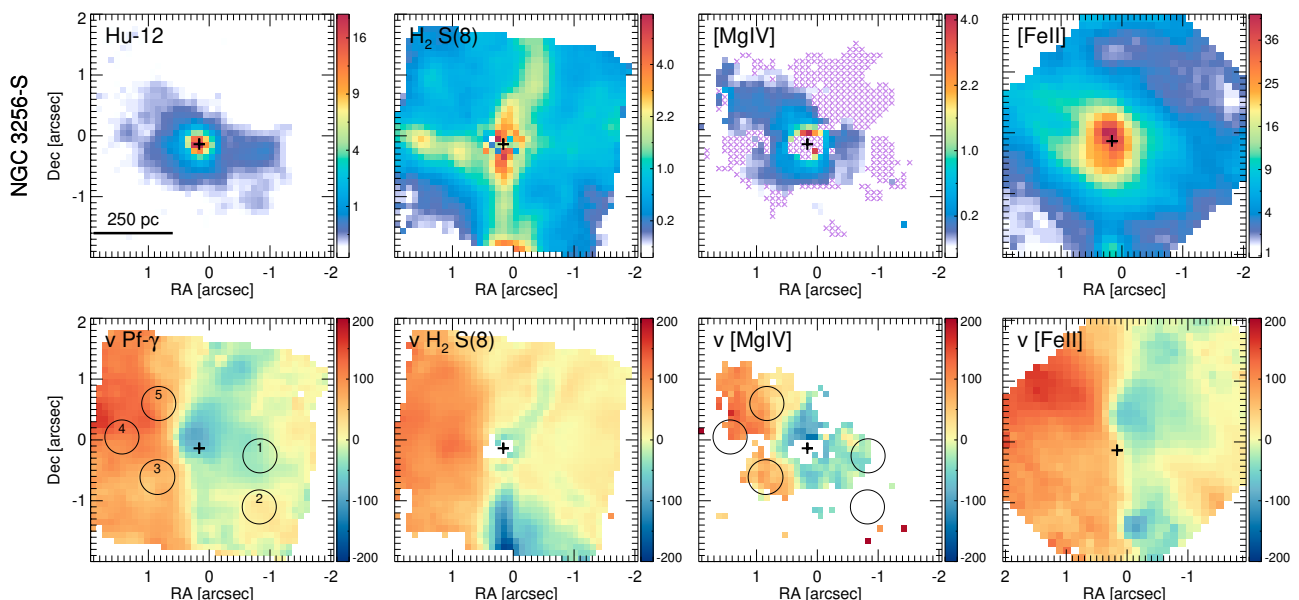


**Fig. 2.** Line maps and velocity fields for NGC 3256 S. The remaining objects are in Figs. A.1-A.4. *Top row from left to right:* Line maps of Hu-12, H<sub>2</sub> S(8), [Mg IV], and [Fe II]. The areas filled with purple crosses in the [Mg IV] panel correspond to regions where the CO  $\nu=1-0$  band is strong and complicates the modeling of the [Mg IV] line. The black cross marks the position of the nucleus. *Bottom row from left to right:* Velocity fields from single Gaussian fits of Pf- $\gamma$ , H<sub>2</sub> S(8), and [Mg IV]. The circles in the first and third panel mark the location and size of the selected regions. The units of the color scale are  $10^{-15} \text{ erg cm}^{-2} \text{ s}^{-1} \text{ arcsec}^{-1}$  for the line maps and  $\text{km s}^{-1}$  for the velocity fields.

ular gas excited by shocks has been identified in interacting systems and U/LIRGs (e.g., Guillard et al. 2009; Pereira-Santaella et al. 2014) but the shock velocities are typically lower than that of the ionizing shocks traced by [Fe II]. We extracted the spectra using a running  $2 \times 2$  spaxels box and fitted a local linear continuum level and a Gaussian profile to determine the flux and velocity at each position (Figs. 2 and A.1-A.4). The [Mg IV] morphology is spatially extended, from few hundreds pc to  $\sim 1$  kpc, and its spatial distribution is more similar to that of the ionized and shocked gas (Hu-12 and [Fe II]) than to the warm molecular H<sub>2</sub> emission. Actually, for the regions selected before, there is a very good linear correlation between the Hu-12 and the [Mg IV] luminosities (excluding the nucleus and outflow of NGC 7469) which spans almost 2 dex and has a Spearman correlation coefficient of 0.94 (Fig. 3 top). This correlation also holds when we consider the individual spaxels (Fig. 3 bottom). The correlation between the shock tracer [Fe II] and [Mg IV] is also good (Fig. C.1 bottom panel). For the warm H<sub>2</sub>, the correlation coefficient is lower, 0.72, and the correlation, if real, would not be linear (Fig. C.1 top panel).

### 3.2. Broad [Mg IV] line profiles

We compared the kinematics of the gas emitting the [Mg IV] line with that of the ionized gas traced by other transitions by modeling their profiles. In particular, we analyzed the following lines in the spectra of the selected regions: the Hu-12 line that is close in wavelength to [Mg IV] and the effects of differential extinction are minimized; Pf- $\gamma$ , which can be more affected by extinction in these dusty galaxies ( $A_{\text{Pf-}\gamma}/A_{[\text{Mg IV}]} = 1.14$ ; Chiar & Tielens 2006), but is intrinsically brighter than Hu-12 ( $\text{Pf-}\gamma/\text{Hu-12} = 5.53$  at 10 000 K; Storey & Hummer 1995); [Fe II] 5.340  $\mu\text{m}$ , which is a good tracer of shocks (Koo et al. 2016); and [Ar II] 6.985  $\mu\text{m}$ , which also traces ionized gas, but has significantly higher signal to noise ratios (SNR).

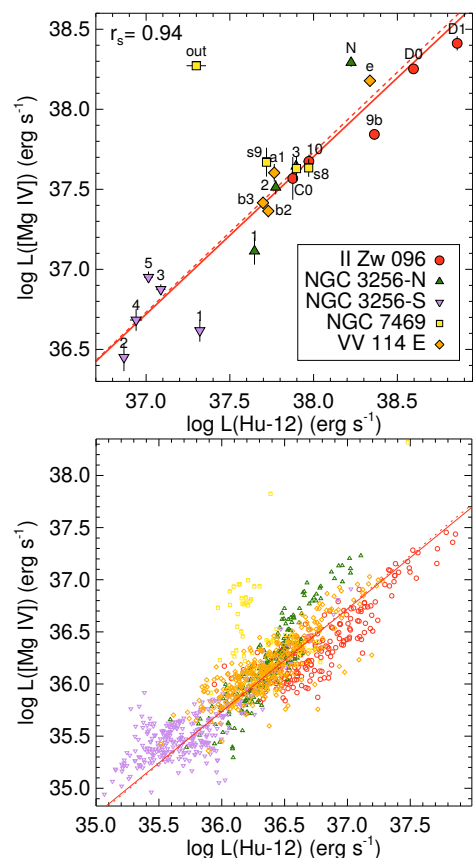


**Fig. 3.** [Mg IV] vs. Hu-12 luminosities of the selected regions (top) and for every spaxel (bottom). Different colors and symbols are used to identify the regions of each object. In the top panel, the labels of the points are the names of the regions. The Spearman correlation coefficient,  $r_s$ , is indicated. The solid and dashed red lines are the best fit ( $\log y = 0.30 + 0.98 \log x$ ) and best linear fit ( $\log y = (-0.29 \pm 0.18) + \log x$ ), respectively, to the luminosities of the regions.

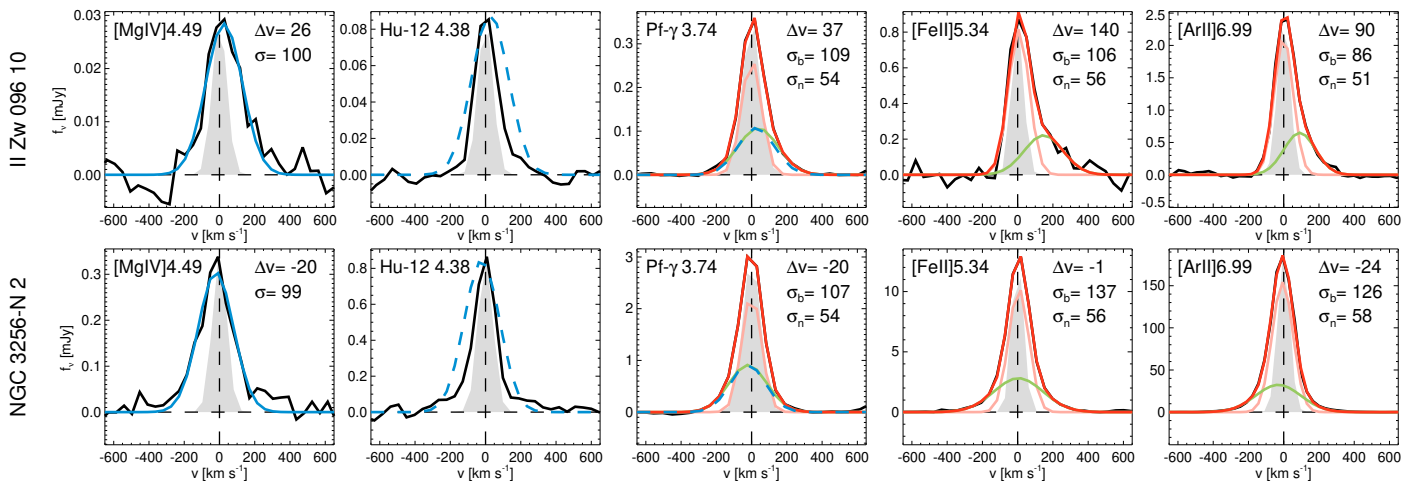


**Fig. 4.** Observed profiles of the [Mg IV], Hu-12, Pf- $\gamma$ , [Fe II], and [Ar II] emission lines (solid black line) for two selected regions. The remaining regions are shown in Fig. B.1. The filled gray Gaussian represents the instrumental spectral resolution. The blue line in the first panel is the best single Gaussian fit to the [Mg IV] profile. The [Mg IV] model is also plotted as a blue dashed line in the second and third panels, normalized to the peak of Hu-12 and the broad Pf- $\gamma$  component, respectively, for reference. The two component fits for Pf- $\gamma$ , [Fe II], and [Ar II], are represented by the pink (narrow component) and green (broad component) lines and the total model in red. The dashed lines mark the rest velocity for each region derived from the narrow component of Pf- $\gamma$  and the zero flux level. The observed (not corrected for instrumental resolution)  $\sigma$  and velocity shift derived from the Gaussian fits are indicated in each panel in  $\text{km s}^{-1}$ .

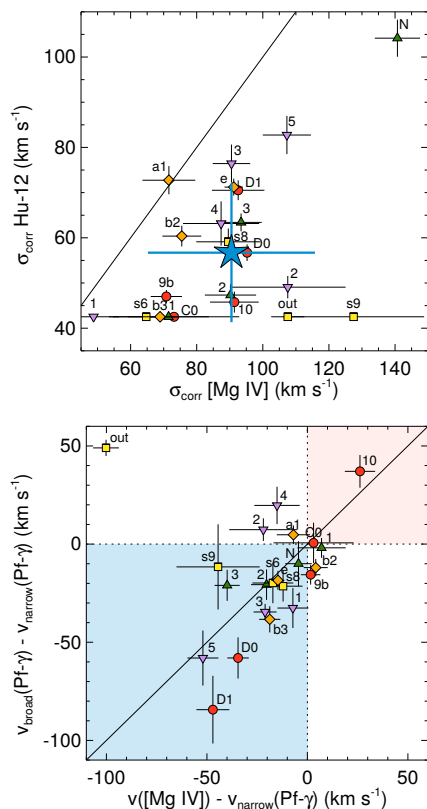


**Fig. 5.** Comparison between the width, corrected for the instrumental resolution, of the [Mg IV] and Hu-12 lines (top) and between the velocity shifts of [Mg IV] and the broad Pf- $\gamma$  component relative to the narrow Pf- $\gamma$  component (bottom). The symbols are as in Fig. 3. The large blue star in the top panel represents the mean  $\sigma_{\text{corr}}$  in each axis. The solid black line is the one-to-one relation. The shaded blue and red areas in the bottom panel indicate blue and red velocity shifts, respectively.

The observed line profiles and best-fit models are presented in Figs. 4 and B.1. A single Gaussian component reproduces well the [Mg IV] and Hu-12 profiles. We find that the [Mg IV]

profile is systematically broader than the Hu-12 profile (top panel of Fig. 5). The average widths, corrected for the instrumental resolution, are:  $\sigma_{\text{corr}}([\text{Mg IV}]) = 90 \pm 25 \text{ km s}^{-1}$  and  $\sigma_{\text{corr}}(\text{Hu} - 12) = 57 \pm 15 \text{ km s}^{-1}$ . In addition, the [Mg IV] emission presents velocity shifts, up to  $\pm 50 \text{ km s}^{-1}$ , with respect to Pf- $\gamma$  (the NIRSspec absolute wavelength accuracy for the G395H grating is  $\sim 12 \text{ km s}^{-1}$ ; priv. comm.). In the higher SNR profiles of Pf- $\gamma$ , a second broader component is clearly detected through higher velocity wings in all the profiles. Wings are also detected in the [Fe II] and [Ar II] lines (Fig. 4, two right most panels). Broad profiles ( $> 200 \text{ km s}^{-1}$ ) have been detected in the mid-IR lines of local U/LIRGs typically associated with the narrow line region (NLR) of AGN and ionized outflows (Spoon et al. 2009; Dasyra et al. 2011; Alonso-Herrero et al. 2013; U et al. 2022; García-Bernete et al. 2022b; Armus et al. 2023). However, we note that the regions selected here are widespread over the entire extent of these objects and not specifically selected to encompass outflows or the NLR of AGN.

We show the best-fit two Gaussian model for these lines in the third, fourth, and fifth columns of Figs. 4 and B.1. We find a remarkable similarity between the widths and velocity shifts of the [Mg IV] and the broad Pf- $\gamma$  profiles. The  $\sigma_{\text{corr}}^{\text{broad}}(\text{Pf-}\gamma) = 105 \pm 15 \text{ km s}^{-1}$  is comparable to  $\sigma_{\text{corr}}([\text{Mg IV}])$  and the great majority (85%) of the velocity shifts have the same sign (i.e., lie in the blue- or red- shaded areas in the bottom panel of Fig. 5).

In most of the cases ( $\sim 75\%$ ) the [Mg IV] line is blue-shifted relative to the narrow component in Pf- $\gamma$ . Although extinction is greatly reduced at  $\sim 4.5 \mu\text{m}$ , it might affect the receding side of the [Mg IV] emission and explain this uneven distribution of the sign of the shifts. A detailed study of the extinction is beyond the scope of this Letter. We also note that the sign of the shifts of the broad component of [Fe II] and [Ar II] follow the same trend (Fig. C.2) and the widths are also comparable to that of the [Mg IV] line,  $\sigma_{\text{corr}}^{\text{broad}}([\text{Fe II}]) = 112 \pm 27 \text{ km s}^{-1}$  and  $\sigma_{\text{corr}}^{\text{broad}}([\text{Ar II}]) = 102 \pm 20 \text{ km s}^{-1}$ .

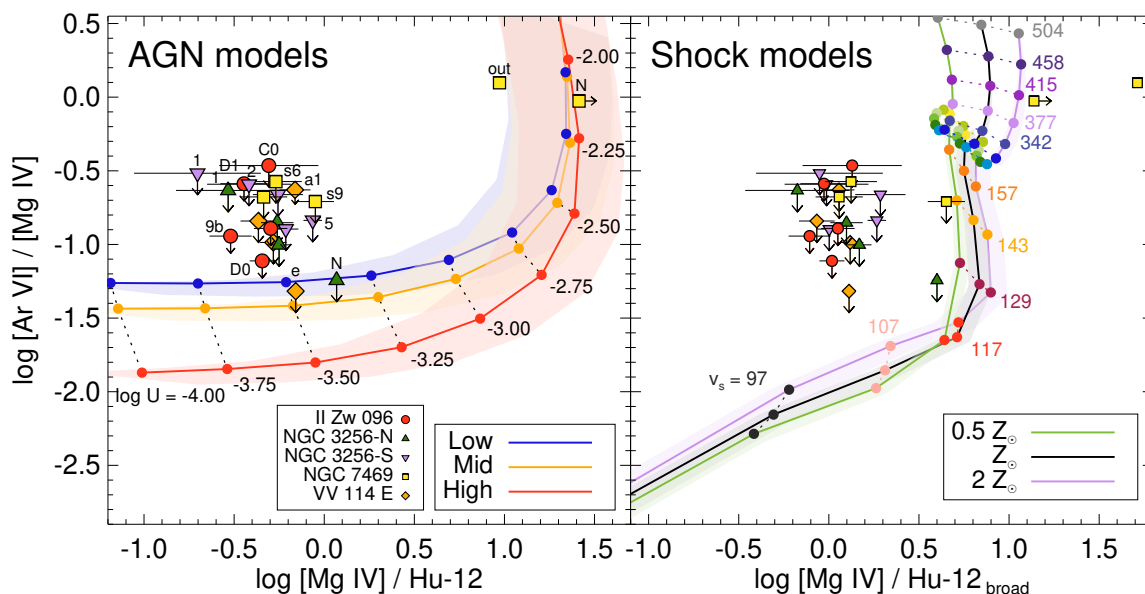


**Fig. 6.**  $[\text{Ar VI}]/[\text{Mg IV}]$  vs.  $[\text{Mg IV}]/\text{Hu-12}$  ratio predicted by AGN (left) and shock (right) models. For the shock models we only consider the flux of the broad component of Hu-12 estimated from the broad to narrow flux ratio of Pf- $\gamma$ . *Left:* The blue, orange, and red solid lines mark the reference AGN models ( $Z_{\odot}$  and  $n_{\text{H}} = 10^3 \text{ cm}^{-3}$ ) for the low, mid, and high Eddington ratio SEDs, respectively. The shaded areas highlight the range of ratios predicted varying the metallicities ( $0.4\text{--}2 Z_{\odot}$ ) and  $n_{\text{H}}$  ( $10^2\text{--}10^5 \text{ cm}^{-3}$ ). Models with the same ionization parameter,  $U$ , are connected by dashed lines. *Right:* The green, black, and purple solid lines mark the reference shock models (ram pressure  $R = 10^6$ ) for  $0.5Z_{\odot}$ ,  $Z_{\odot}$ , and  $2Z_{\odot}$  metallicities, respectively. The shaded areas highlight the range of ratios predicted varying  $R$  ( $10^4\text{--}10^8$ ). Models with the same shock velocity,  $v_s$ , are connected by dashed lines. The observed ratios use the same symbols as in Fig. 3. The models are described in Sect. 4 and Appendix D.

#### 4. Origin of the [Mg iv] emission: star-formation, AGN, and shock models

Despite its high IP, the results described in Sect. 3 are not fully consistent with an AGN origin of the [Mg iv] emission because: (1) it is extended and correlated with the Hu-12 emission, a H recombination line tracing star forming regions based on its morphology; (2) the [Ar vi] line, with a slightly lower IP and typically found in other AGN, is undetected, except in the outflow and nucleus of the Type 1 AGN; and (3) the [Mg iv] profile is broader and shifted compared to the other transitions. Therefore, we created three grids of models (star-formation, AGN, and shocks) to investigate the origin of the [Mg iv] emission. We briefly describe the models in this section and provide further details in Appendix D.

We modeled the emission from gas photoionized by AGN or star-formation using the spectral synthesis code CLOUDY (Chatzikos et al. 2023). We mostly followed Pereira-Santaella et al. (2017) to create these grids but updated the spectral energy distributions (SEDs) of the incident radiation field. For the star-formation grids, we used the Binary Population and Spectral Synthesis (BPASS) library (Eldridge et al. 2017), which includes stripped-envelope stars that have harder ionizing spectra (e.g., Göteborg et al. 2019) and could contribute to the [Mg iv] emission. For the AGN models, we used the three SEDs for low, medium, and high Eddington ratios derived by Jin et al. (2012), which provide a more realistic approximation to the intrinsic SED of AGN than a power-law.

Based on these grids, we can reject that the [Mg iv] line originates in gas photoionized by stars since the observed [Mg iv]/Hu-12 ratio ( $\sim 0.5$ ; Fig. 3) is  $>2.3$  dex larger than the predicted ratio (Fig. D.1).

The AGN photoionization predictions for the [Mg iv]/Hu-12 and [Ar vi]/[Mg iv] ratios are shown in the left panel of Fig. 6. The outflow and nucleus of the Sy1 NGC 7469 lie close to the

grid with ionization parameters,  $\log U$ , between  $-2.00$  and  $-2.25$  in the range of Seyfert AGN (e.g., Pérez-Díaz et al. 2022). For the remaining regions, the lower [Mg iv]/Hu-12 ratio and the non-detection of [Ar vi] would imply  $\log U < -3.25$ , which is low but is also found in some AGN and low-ionization nuclear emission regions (LINERs; e.g., Thomas et al. 2018).

Finally, we created a grid of shock models using MAPPINGS V following Sutherland & Dopita (2017), which includes several improvements compared to the models in Allen et al. (2008) (see Appendix D.3). The [Mg iv]/Hu-12<sub>broad</sub> ratio and the [Ar vi]  $3\sigma$  upper limit are compatible with the emission produced by shocks with shock velocities  $v_s = 100\text{--}130 \text{ km s}^{-1}$  (Fig. 6 right). The  $v_s$  is not directly equivalent to  $\sigma_{\text{corr}}$  (e.g., Ho et al. 2014; Perna et al. 2020), however, the fact that they are similar,  $\sigma_{\text{corr}}([\text{Mg IV}]) = 90 \pm 25 \text{ km s}^{-1}$  (Sect. 3.2), supports that shocks are a possible origin of the [Mg iv] emission.

In summary, while we cannot completely reject the AGN origin in a very low  $\log U$  environment based on these line ratios, the morphology and kinematic properties of the [Mg iv] emission (broader profile and velocity shifts) favor the shock origin. Under this assumption, the good correlation between the extended [Mg iv] emission and the recombination line Hu-12, which traces star forming clumps, is naturally explained if the shocks producing the [Mg iv] emissions are powered by supernove (SNe). To estimate if the energy released by SNe can produce the observed [Mg iv] luminosity relative to the star-formation rate (i.e., [Mg iv]/Hu-12 ratio), we combined stellar population evolution models and the shock models. Shock models predict efficient [Mg iv] emission at  $v_s \sim 110\text{--}160 \text{ km s}^{-1}$ , so observing [Mg iv] emission at these velocities is also favored (Fig. D.3). Using these relations (see Appendix D.4), the predicted  $\log [\text{Mg IV}]/\text{Hu-12}$  ratio from a star forming region with shocks produced by SNe is between  $-1.4$  and  $-0.5$ . The observed  $\log [\text{Mg IV}]/\text{Hu-12}$  ratio,  $-0.29 \pm 0.18$ , lies at the upper end of the range but is consis-

tent with it considering the relatively large uncertainties of both the shock models (e.g.,  $v_s$ , Mg abundance) and the star-formation models (e.g., initial mass function, energy per SN, electron temperature). Therefore, it is plausible that SNe can provide enough mechanical energy to generate the observed [Mg iv] emission.

## 5. Summary and conclusions

Using *JWST*/NIRSpec integral field spectroscopy, we investigated the extended high-ionization [Mg iv] 4.487  $\mu\text{m}$  (IP 80 eV) emission in a sample of four local LIRGs, only one of them hosting a Seyfert-like AGN. Excluding the nucleus and outflow of this AGN, we find that shocks related to star formation are the most likely origin of the extended [Mg iv] emission since: (1) the [Mg iv] luminosity is well correlated with the recombination line Hu-12 4.376  $\mu\text{m}$ , which traces star forming clumps in these objects; and the [Ar vi] 4.530  $\mu\text{m}$  line (IP 75 eV), which is common in the spectra of AGN, remains undetected; and (2) the [Mg iv] profile is broader ( $\sigma_{\text{corr}}(\text{[Mg iv]}) = 90 \pm 25 \text{ km s}^{-1}$ ) and shifted up to  $\pm 50 \text{ km s}^{-1}$  relative to the recombination lines ( $\sigma_{\text{corr}}(\text{Hu-12}) = 57 \pm 15 \text{ km s}^{-1}$ ). The [Mg iv] line kinematics actually track the faint wings of the lower ionization lines (P $\gamma$  3.741  $\mu\text{m}$ , [Fe ii] 5.340  $\mu\text{m}$ , and [Ar ii] 6.985  $\mu\text{m}$ ) and resembles the large scale rotating velocity field of the galaxies.

Supporting this interpretation, shock models with  $v_s \sim 100$ – $130 \text{ km s}^{-1}$  (i.e., similar to the  $\sigma$  of [Mg iv] and the broad component in other species) are consistent with the observed [Mg iv]/Hu-12 ratio and the [Ar vi] upper limit. Also, the [Mg iv] luminosity is comparable to that expected from shocks associated with the mechanical energy released by SNe in these regions. Based on these results, the detection of [Mg iv] emission is expected in pure star-forming galaxies, at least in objects with high gas and star-formation surface densities similar to those of local LIRGs (e.g., Sánchez-García et al. 2022).

Due to its high IP, [Mg iv] offers a unique view of the shocked gas by tracing the highly ionized phase, contrasting with classic shock tracers such as the [Fe ii] transitions, which have a lower IP of 7.9 eV and are more easily ionized. Compared to the [O iv] 25.9  $\mu\text{m}$  line (IP 55 eV), the higher sensitivity and angular and spectral resolutions of *JWST* at the shorter wavelength of the [Mg iv] line will be beneficial for future studies of stellar feedback caused by these widespread shocks in strong starbursts.

*Acknowledgements.* We thank the referee for their useful comments and suggestions. The authors acknowledge the GOALS ERS team for developing their observing program. MPS acknowledges support from grant RYC2021-033094-I funded by MICIU/AEI/10.13039/501100011033 and the European Union NextGenerationEU/PRTR. IGB and DR acknowledge support from STFC through grants ST/S000488/1 and ST/W000903/1. AAH acknowledges support from grant PID2021-124665NB-I00 funded by the Spanish Ministry of Science and Innovation and the State Agency of Research MCIN/AEI/10.13039/501100011033 and ERDF A way of making Europe. This work is based on observations made with the NASA/ESA/CSA James Webb Space Telescope. The data were obtained from the Mikulski Archive for Space Telescopes at the Space Telescope Science Institute, which is operated by the Association of Universities for Research in Astronomy, Inc., under NASA contract NAS 5-03127 for *JWST*; and from the European *JWST* archive (e*JWST*) operated by the ESAC Science Data Centre (ESDC) of the European Space Agency. These observations are associated with program #1328.

## References

Allen, M. G., Groves, B. A., Dopita, M. A., Sutherland, R. S., & Kewley, L. J. 2008, *ApJS*, 178, 20  
 Alonso-Herrero, A., Pereira-Santaella, M., Rieke, G. H., et al. 2013, *ApJ*, 765, 78

Alonso-Herrero, A., Pereira-Santaella, M., Rieke, G. H., & Rigopoulou, D. 2012, *ApJ*, 744, 2  
 Argyriou, I., Glasse, A., Law, D. R., et al. 2023, *A&A*, 675, A111  
 Armus, L., Lai, T., U, V., et al. 2023, *ApJ*, 942, L37  
 Armus, L., Mazzarella, J. M., Evans, A. S., et al. 2009, *PASP*, 121, 559  
 Barcos-Muñoz, L., Leroy, A. K., Evans, A. S., et al. 2017, *ApJ*, 843, 117  
 Bianchin, M., U, V., Song, Y., et al. 2023, arXiv e-prints, arXiv:2308.00209  
 Böker, T., Arribas, S., Lützgendorf, N., et al. 2022, *A&A*, 661, A82  
 Bushouse, H., Eisenhamer, J., Dencheva, N., et al. 2023, *JWST Calibration Pipeline*  
 Chatzikos, M., Bianchi, S., Camilloni, F., et al. 2023, *Rev. Mexicana Astron. Astrofis.*, 59, 327  
 Chiar, J. E. & Tielens, A. G. G. M. 2006, *ApJ*, 637, 774  
 Corrales, L. R., García, J., Wilms, J., & Baganoff, F. 2016, *MNRAS*, 458, 1345  
 Dasyra, K. M., Ho, L. C., Netzer, H., et al. 2011, *ApJ*, 740, 94  
 Del Zanna, G., Dere, K. P., Young, P. R., & Landi, E. 2021, *ApJ*, 909, 38  
 Diamond-Stanic, A. M., Rieke, G. H., & Rigby, J. R. 2009, *ApJ*, 698, 623  
 Donnan, F. R., García-Bernete, I., Rigopoulou, D., et al. 2023, *MNRAS*, 519, 3691  
 Eldridge, J. J., Stanway, E. R., Xiao, L., et al. 2017, *PASA*, 34, e058  
 Falstad, N., Aalto, S., König, S., et al. 2021, *A&A*, 649, A105  
 Ferland, G. J., Done, C., Jin, C., Landt, H., & Ward, M. J. 2020, *MNRAS*, 494, 5917  
 García-Bernete, I., Alonso-Herrero, A., Rigopoulou, D., et al. 2024a, *A&A*, 681, L7  
 García-Bernete, I., Pereira-Santaella, M., González-Alfonso, E., et al. 2024b, *A&A*, 682, L5  
 García-Bernete, I., Ramos Almeida, C., Acosta-Pulido, J. A., et al. 2016, *MNRAS*, 463, 3531  
 García-Bernete, I., Rigopoulou, D., Aalto, S., et al. 2022a, *A&A*, 663, A46  
 García-Bernete, I., Rigopoulou, D., Alonso-Herrero, A., et al. 2022b, *MNRAS*, 509, 4256  
 González-Alfonso, E., García-Bernete, I., Pereira-Santaella, M., et al. 2024, *A&A*, 682, A182  
 Götzberg, Y., de Mink, S. E., Groh, J. H., Leitherer, C., & Norman, C. 2019, *A&A*, 629, A134  
 Guillard, P., Boulanger, F., Pineau Des Forêts, G., & Appleton, P. N. 2009, *A&A*, 502, 515  
 Hayashi, T. J., Hagiwara, Y., & Imanishi, M. 2021, *MNRAS*, 504, 2675  
 Ho, I. T., Kewley, L. J., Dopita, M. A., et al. 2014, *MNRAS*, 444, 3894  
 Inami, H., Surace, J., Armus, L., et al. 2022, *ApJ*, 940, L6  
 Jakobsen, P., Ferruit, P., Alves de Oliveira, C., et al. 2022, *A&A*, 661, A80  
 Jin, C., Ward, M., & Done, C. 2012, *MNRAS*, 425, 907  
 Koo, B.-C., Raymond, J. C., & Kim, H.-J. 2016, *Journal of Korean Astronomical Society*, 49, 109  
 Kroupa, P. 2001, *MNRAS*, 322, 231  
 Lutz, D., Kunze, D., Spoon, H. W. W., & Thornley, M. D. 1998, *A&A*, 333, L75  
 Lykins, M. L., Ferland, G. J., Kisielius, R., et al. 2015, *ApJ*, 807, 118  
 Mouri, H., Kawara, K., & Taniguchi, Y. 2000, *ApJ*, 528, 186  
 Nardini, E., Risaliti, G., Salvati, M., et al. 2009, *MNRAS*, 399, 1373  
 Ohyama, Y., Terashima, Y., & Sakamoto, K. 2015, *ApJ*, 805, 162  
 Osterbrock, D. E. & Martel, A. 1993, *ApJ*, 414, 552  
 Patton, D. R., Wilson, K. D., Metrow, C. J., et al. 2020, *MNRAS*, 494, 4969  
 Pereira-Santaella, M., Alonso-Herrero, A., Rieke, G. H., et al. 2010a, *ApJS*, 188, 447  
 Pereira-Santaella, M., Álvarez-Márquez, J., García-Bernete, I., et al. 2022, *A&A*, 665, L11  
 Pereira-Santaella, M., Colina, L., García-Burillo, S., et al. 2021, *A&A*, 651, A42  
 Pereira-Santaella, M., Diamond-Stanic, A. M., Alonso-Herrero, A., & Rieke, G. H. 2010b, *ApJ*, 725, 2270  
 Pereira-Santaella, M., González-Alfonso, E., García-Bernete, I., García-Burillo, S., & Rigopoulou, D. 2024, *A&A*, 681, A117  
 Pereira-Santaella, M., Rigopoulou, D., Farrah, D., Lebouteiller, V., & Li, J. 2017, *MNRAS*, 470, 1218  
 Pereira-Santaella, M., Spinoglio, L., van der Werf, P. P., & Piqueras López, J. 2014, *A&A*, 566, A49  
 Pérez-Díaz, B., Pérez-Montero, E., Fernández-Ontiveros, J. A., & Vílchez, J. M. 2022, *A&A*, 666, A115  
 Perna, M., Arribas, S., Catalán-Torrecilla, C., et al. 2020, *A&A*, 643, A139  
 Petric, A. O., Armus, L., Howell, J., et al. 2011, *ApJ*, 730, 28  
 Rich, J., Aalto, S., Evans, A. S., et al. 2023, *ApJ*, 944, L50  
 Rigby, J. R. & Rieke, G. H. 2004, *ApJ*, 606, 237  
 Rogantini, D., Costantini, E., Zeegers, S. T., et al. 2020, *A&A*, 641, A149  
 Sánchez-García, M., Pereira-Santaella, M., García-Burillo, S., et al. 2022, *A&A*, 659, A102  
 Satyapal, S., Kamal, L., Cann, J. M., Secrest, N. J., & Abel, N. P. 2021, *ApJ*, 906, 35  
 Spoon, H. W. W., Armus, L., Marshall, J. A., et al. 2009, *ApJ*, 693, 1223  
 Stierwalt, S., Armus, L., Surace, J. A., et al. 2013, *ApJS*, 206, 1  
 Storey, P. J. & Hummer, D. G. 1995, *MNRAS*, 272, 41

- Sturm, E., Lutz, D., Verma, A., et al. 2002, *A&A*, 393, 821  
Sutherland, R. S. & Dopita, M. A. 2017, *ApJS*, 229, 34  
Thomas, A. D., Dopita, M. A., Kewley, L. J., et al. 2018, *ApJ*, 856, 89  
U, V., Lai, T., Bianchin, M., et al. 2022, *ApJ*, 940, L5  
Veilleux, S., Rupke, D. S. N., Kim, D.-C., et al. 2009, *ApJS*, 182, 628  
Weinberger, R., Springel, V., Pakmor, R., et al. 2018, *MNRAS*, 479, 4056  
Wright, G. S., Rieke, G. H., Glasse, A., et al. 2023, *PASP*, 135, 048003  
Zapartas, E., de Mink, S. E., Izzard, R. G., et al. 2017, *A&A*, 601, A29

- 
- <sup>1</sup> Instituto de Física Fundamental, CSIC, Calle Serrano 123, 28006 Madrid, Spain  
e-mail: miguel.pereira@iff.csic.es
- <sup>2</sup> Department of Physics, University of Oxford, Keble Road, Oxford OX1 3RH, UK
- <sup>3</sup> Universidad de Alcalá, Departamento de Física y Matemáticas, Campus Universitario, 28871 Alcalá de Henares, Madrid, Spain
- <sup>4</sup> Centro de Astrobiología (CAB), CSIC-INTA, Camino Bajo del Castillo s/n, E-28692 Villanueva de la Cañada, Madrid, Spain
- <sup>5</sup> Centro de Astrobiología (CAB), CSIC-INTA, Ctra de Torrejón a Ajalvir, km 4, 28850, Torrejón de Ardoz, Madrid, Spain
- <sup>6</sup> Observatorio Astronómico Nacional (OAN-IGN)-Observatorio de Madrid, Alfonso XII, 3, 28014, Madrid, Spain
- <sup>7</sup> School of Sciences, European University Cyprus, Diogenes street, Engomi, 1516 Nicosia, Cyprus

## Appendix A: Emission line maps

Figs. A.1-A.4 show the emission maps for the complete sample.

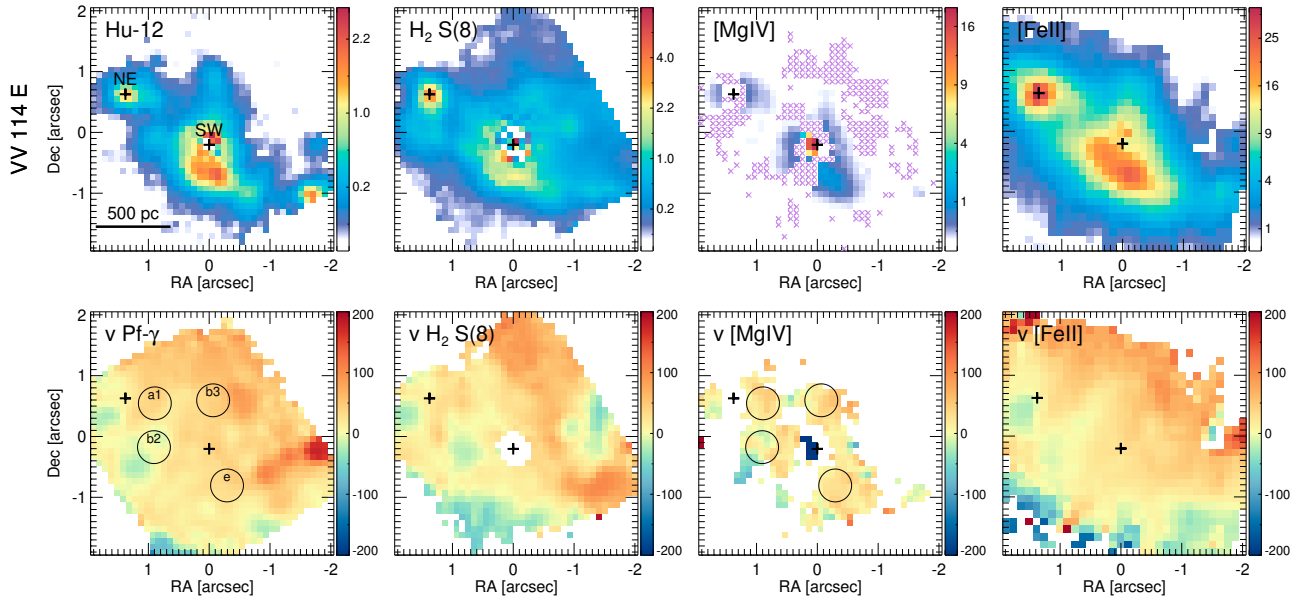


Fig. A.1. Same as Fig. 2 but for VV 114 E.

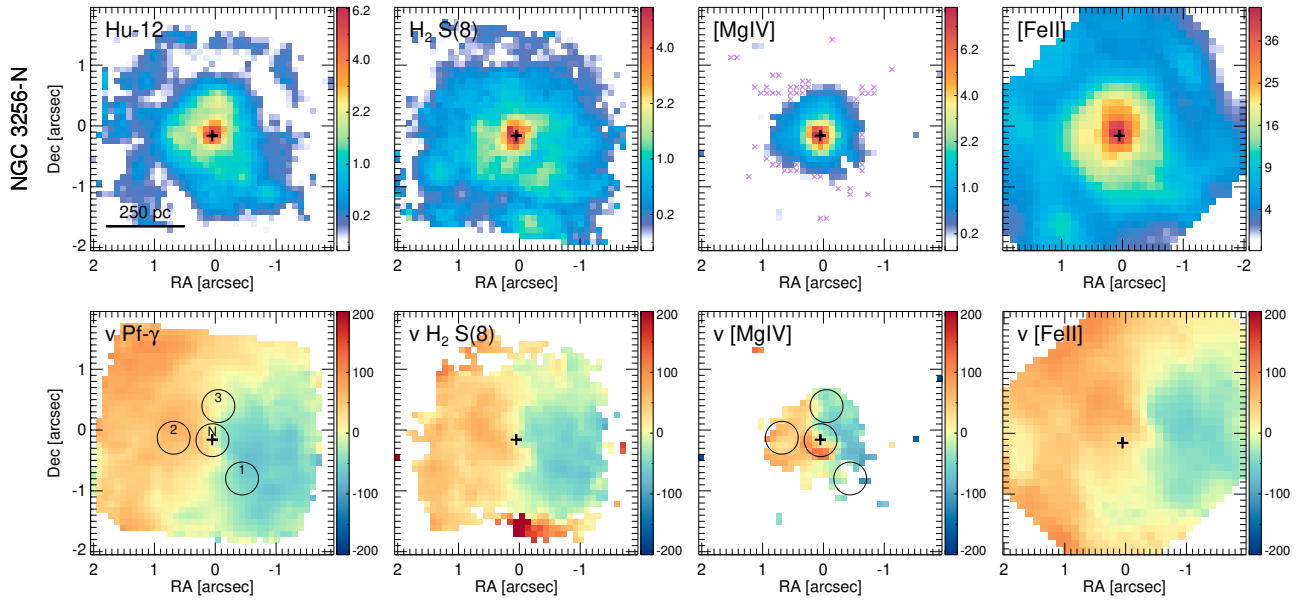


Fig. A.2. Same as Fig. 2 but for NGC 3256 N.

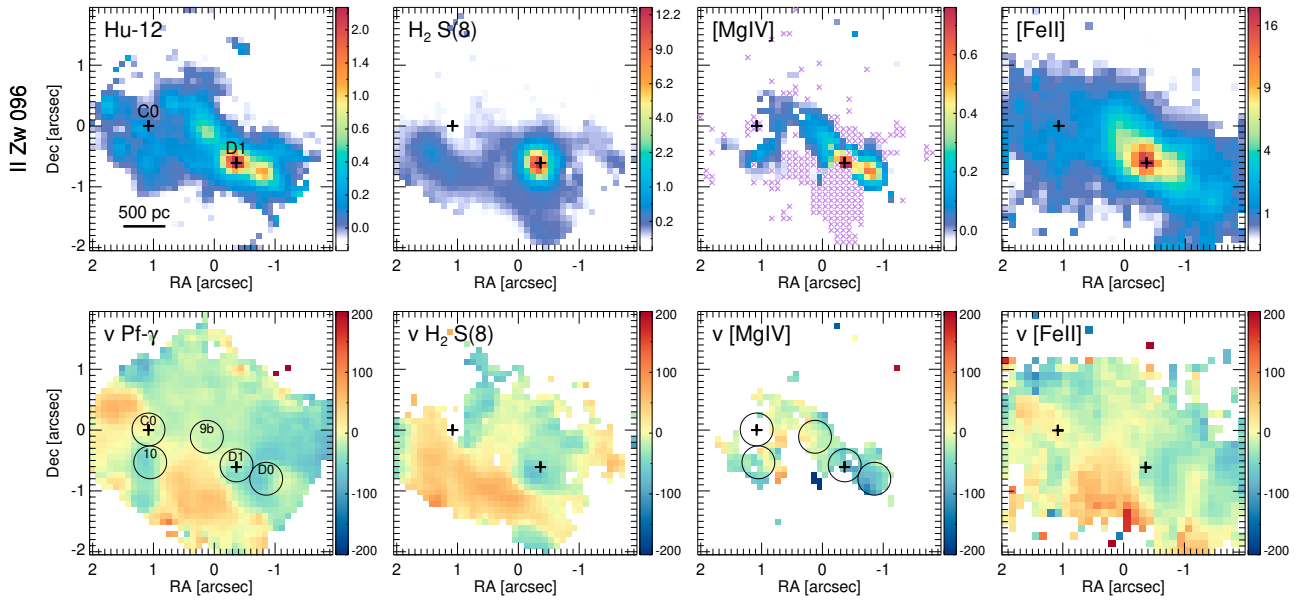


Fig. A.3. Same as Fig. 2 but for II Zw 096.

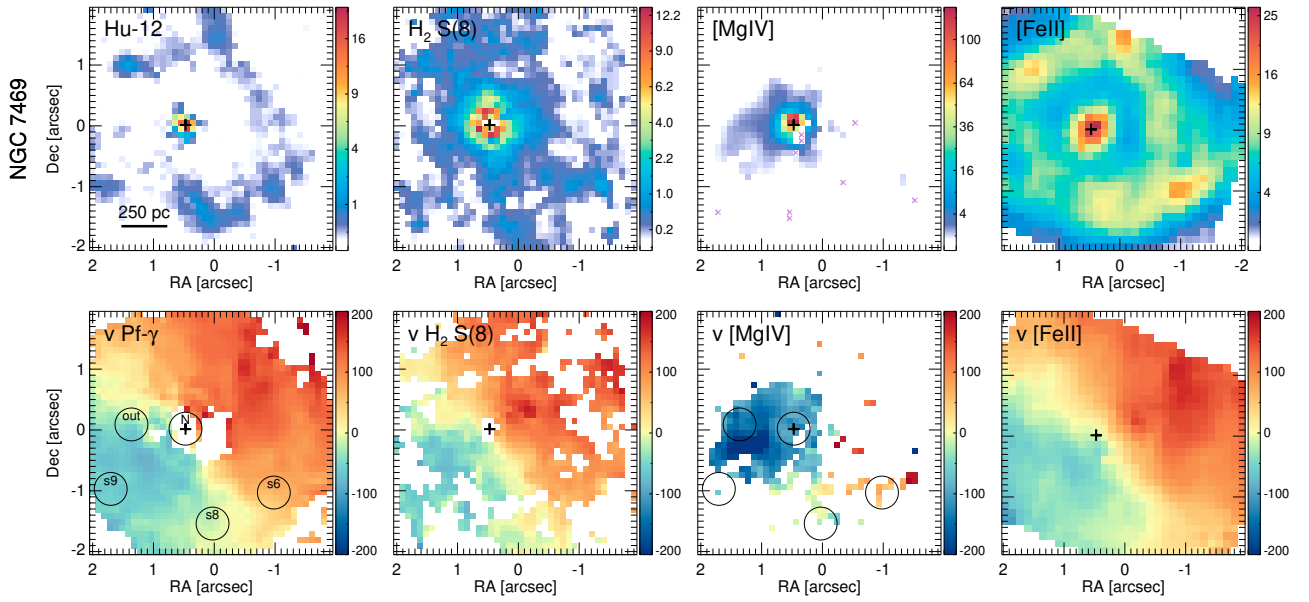


Fig. A.4. Same as Fig. 2 but for NGC 7469.

## Appendix B: Emission line profiles

Fig. B.1 shows the emission line profiles for all the selected regions.

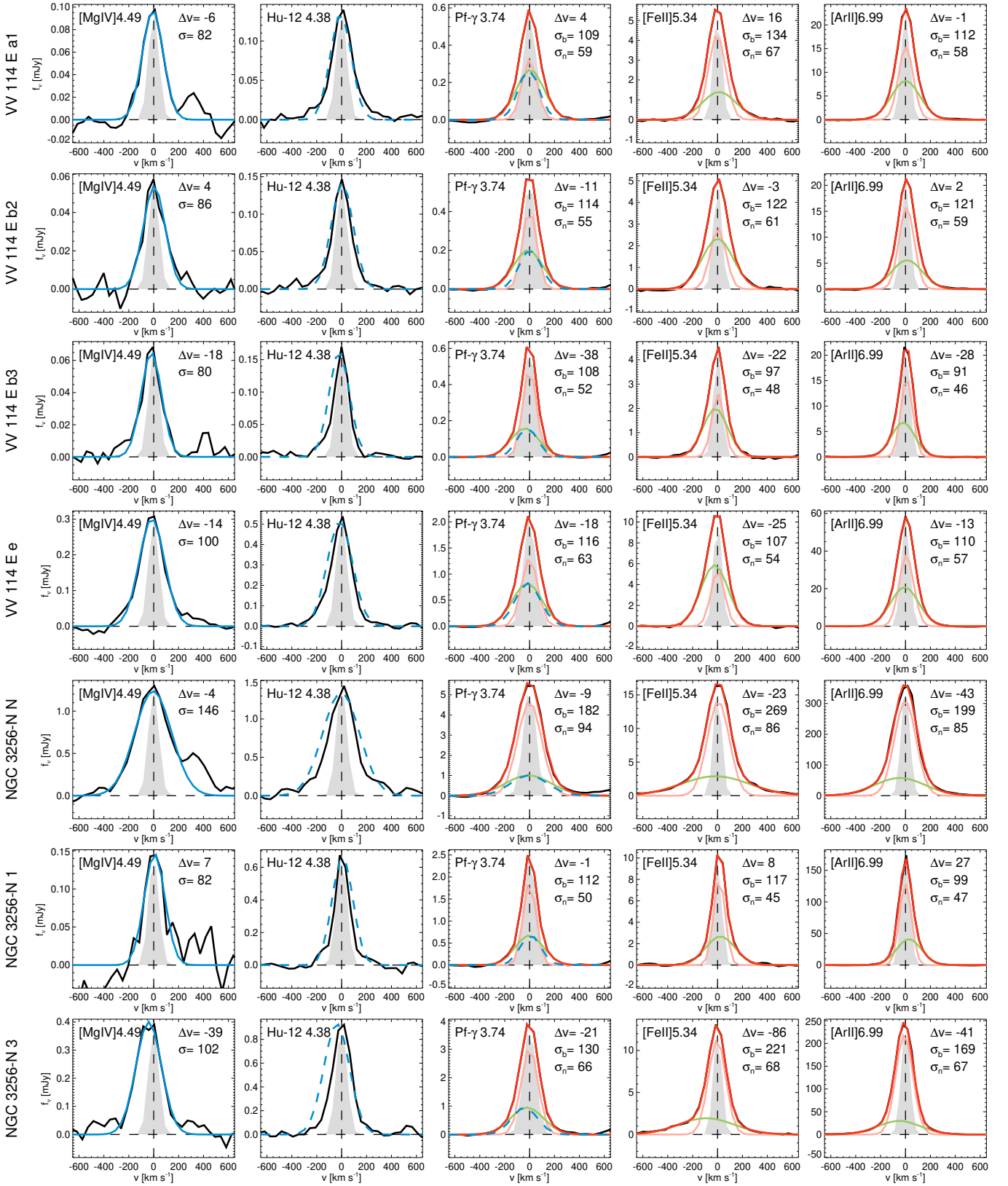


Fig. B.1. Continued.

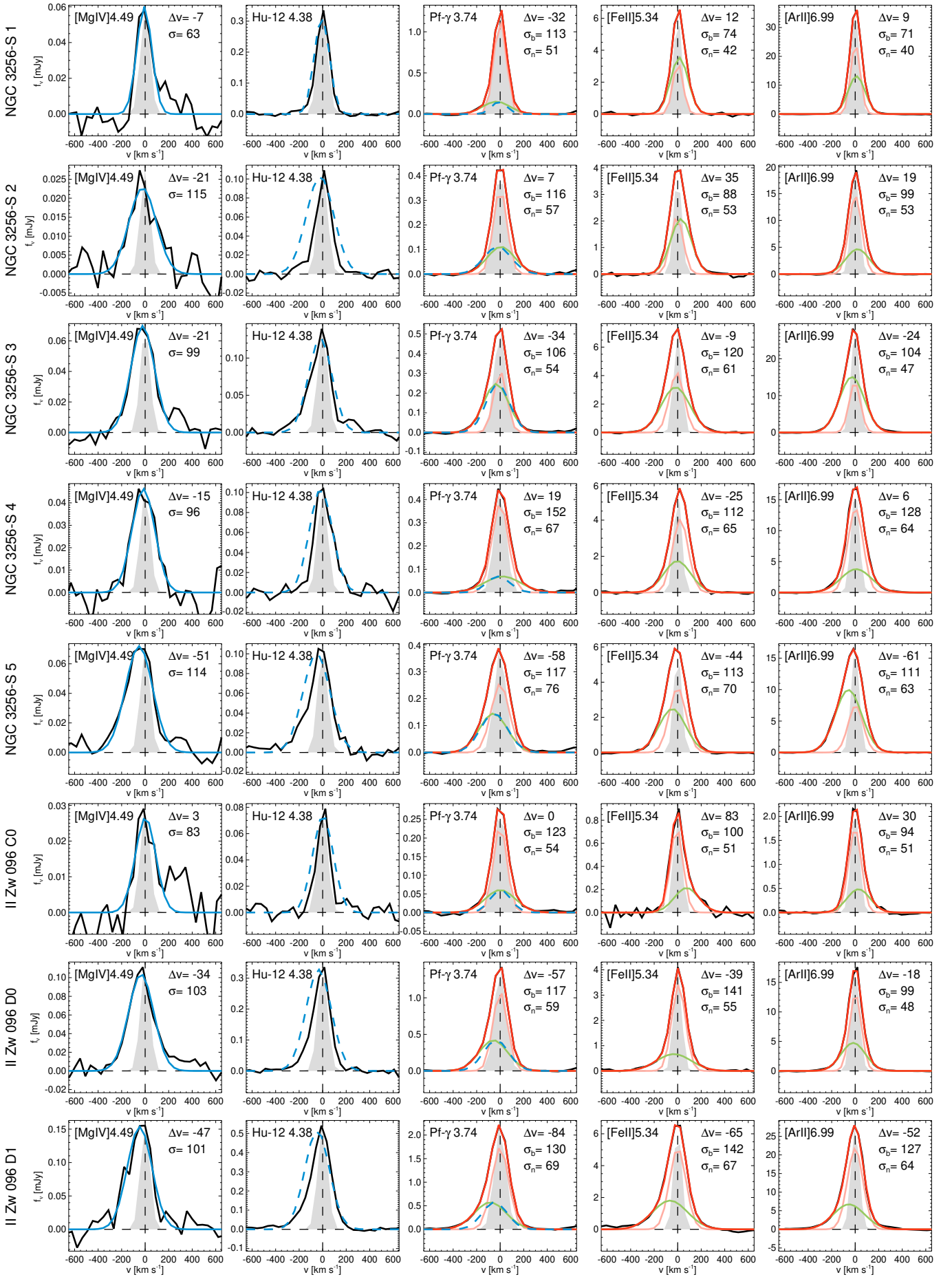


Fig. B.1. Continued.

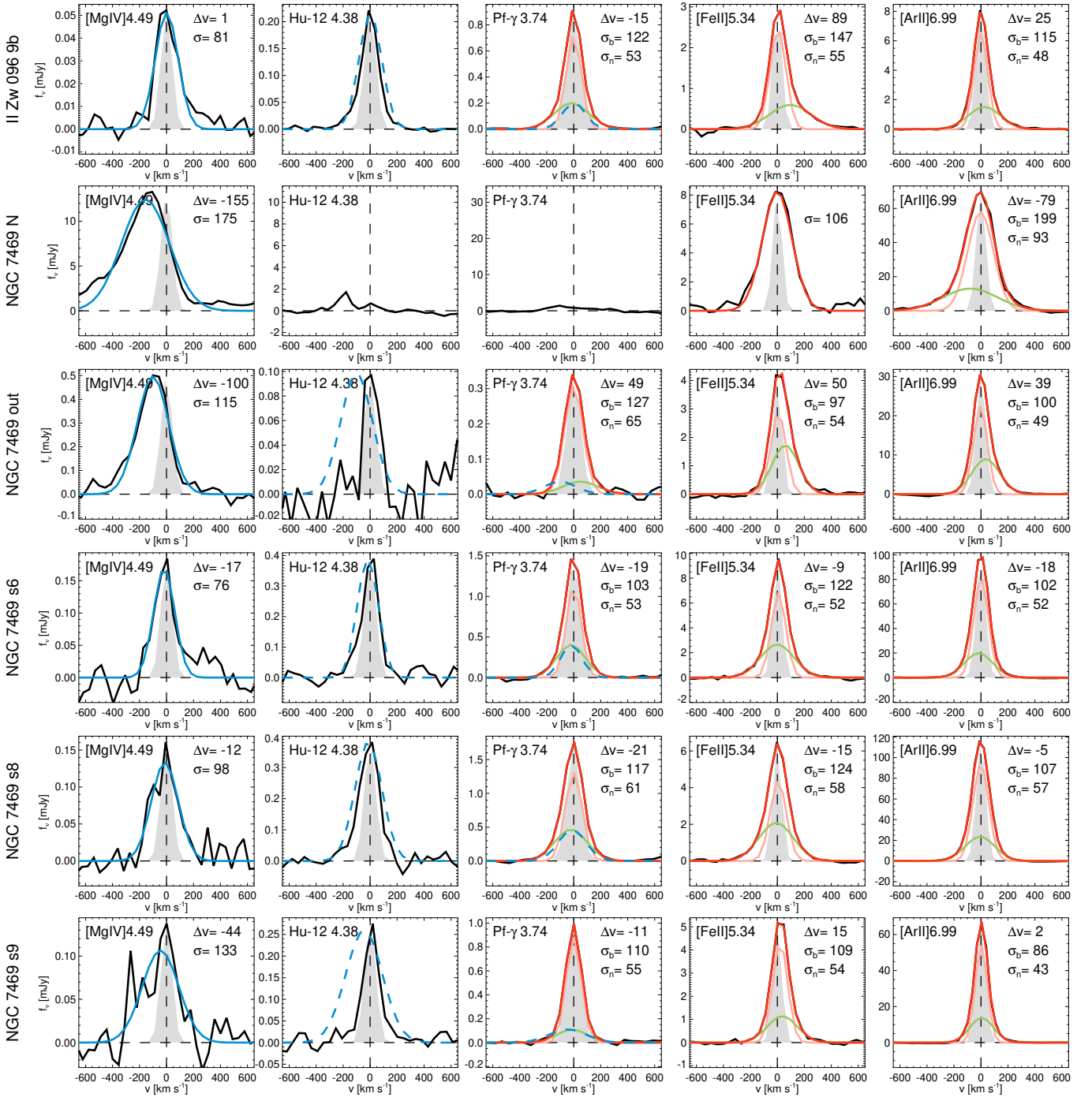
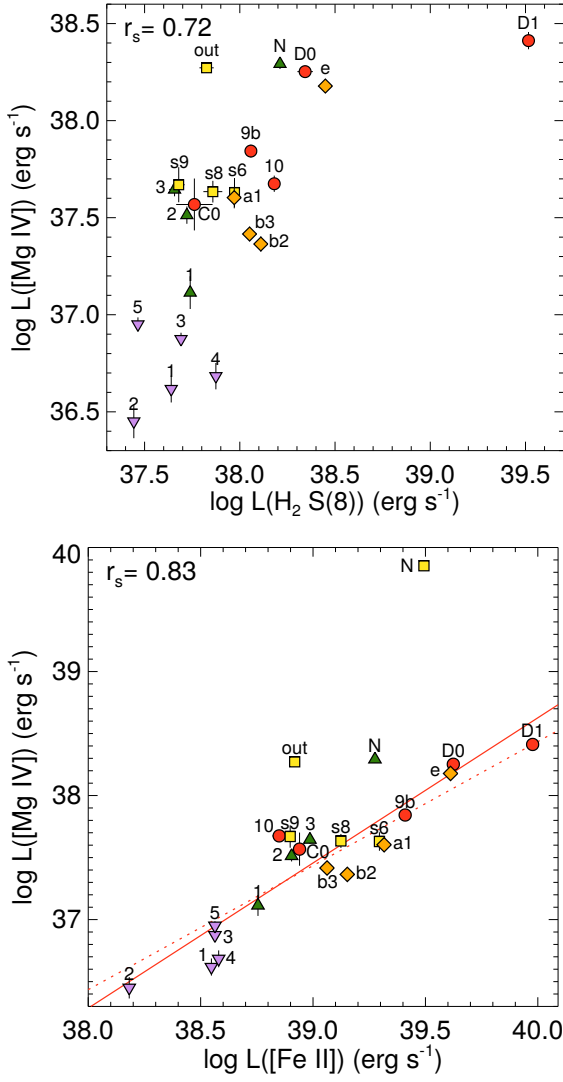


Fig. B.1. Continued.



**Fig. C.1.** [Mg IV] vs. H<sub>2</sub> S(8) (top) and vs. [Fe II] (bottom) luminosities. The symbols are as in Fig. 3. The solid red line is the best fit ( $\log y = -8.20 + 1.17 \log x$ ) and the dashed red line the best linear fit ( $\log y = (-1.56 \pm 0.25) + \log x$ ).

### Appendix C: Relation between the luminosity and kinematics of [Mg IV] and H<sub>2</sub> S(8), [Fe II], and [Ar II]

Fig. C.1 shows the relation between the [Mg IV] and the H<sub>2</sub> S(8) and [Fe II] 5.34  $\mu$ m luminosities. We scaled the MRS spectra to match the NIRSPEC continuum at  $\sim 5 \mu$ m. The scaling factors are between 0.7 and 1.3. We did not correct for the differential extinction affecting these lines. Fig. C.2 presents the comparison between the [Mg IV] line kinematics observed with JWST/NIRSPEC and the longer wavelength lines ([Fe II] and [Ar II]) observed with JWST/MRS.

### Appendix D: Star-formation, AGN, and shock models

In this section, we present a more detailed description of the grids of models used in Sect. 4. For the star-formation and AGN photoionization models, we used CLOUDY version 23.01 (Chatzikos et al. 2023) and mostly followed Pereira-Santaella et al. (2017) to create the grids. The main differences are the updated SEDs used for the incident radiation field (see below). For

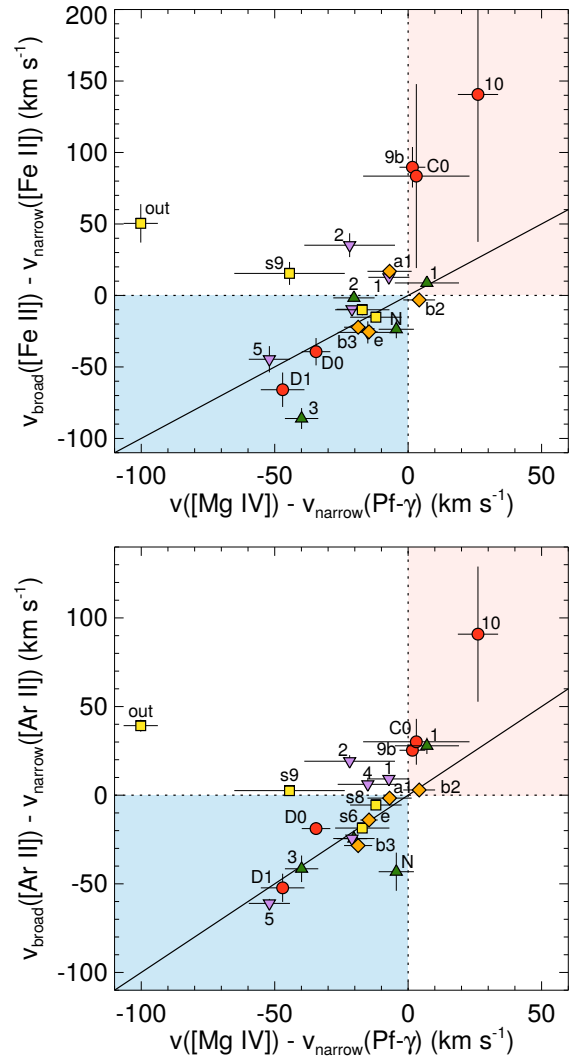


**Fig. C.2.** Same as the bottom panel of Fig. 5 but for [Fe II] (top) and [Ar II] (bottom).

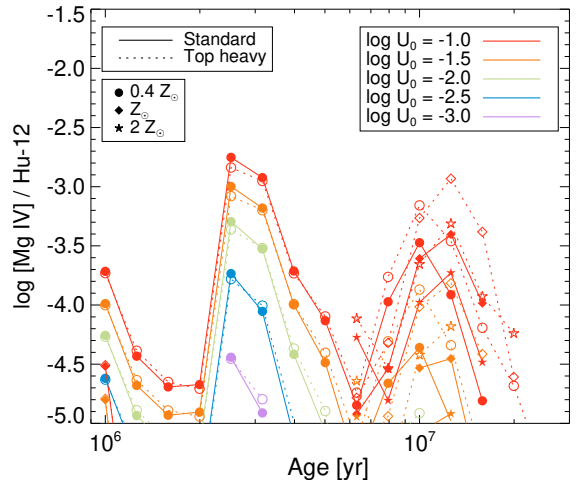


**Fig. D.1.** [Mg IV]/Hu-12 ratio for an instantaneous burst of star-formation as function of the stellar age. The circles, diamonds, and stars mark the ratios for  $0.4Z_{\odot}$ ,  $Z_{\odot}$ , and  $2Z_{\odot}$ . The filled (empty) symbols connected by a solid (dashed) line corresponds to a standard (top heavy) IMF. The grid with  $n_{\text{H}} = 10^2 \text{ cm}^{-3}$  is plotted. The color of the lines indicates the ionization parameter,  $U_0$ .

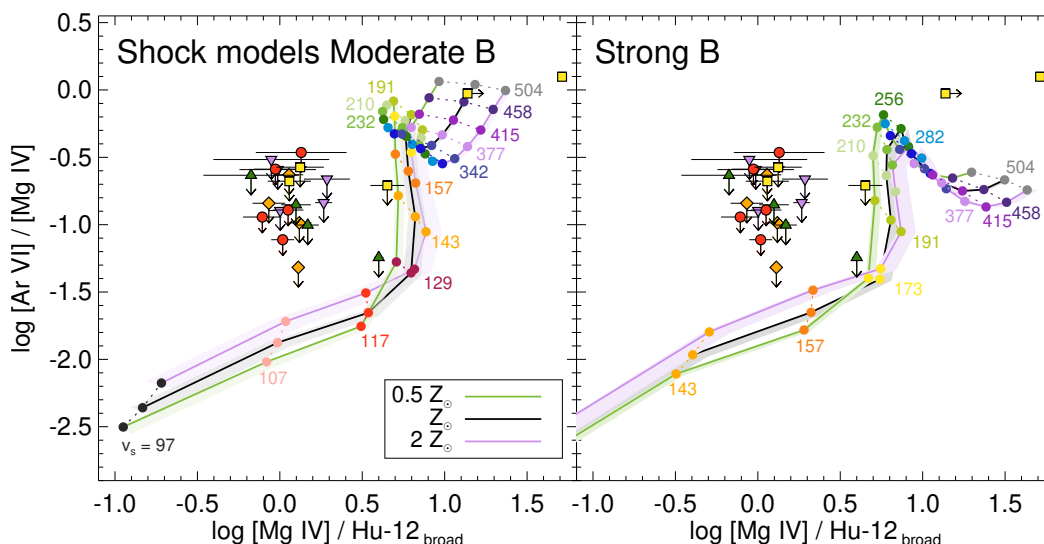


**Fig. D.2.** Same as the right panel of Fig. 6 but for the moderate (left) and strong (right) magnetic field cases.

the shock models, we used the MAPPINGS V code version 5.2.0 following Sutherland & Dopita (2017).

#### D.1. Star-formation models

We used a constant density slab model. The incident radiation field is obtained from the BPASS library (version 2.2; Eldridge et al. 2017). This library includes the effect of stripped-envelope stars in binary systems, which increase the hardness of the spectrum. We assumed an instantaneous burst of star-formation with ages between  $10^6$  to  $10^8$  with 0.1 dex steps. We considered three stellar metallicities ( $0.4 Z_{\odot}$ ,  $Z_{\odot}$ , and  $2 Z_{\odot}$ ), and two initial mass functions (IMFs), both with an upper stellar mass limit of  $300 M_{\odot}$ : a standard Kroupa (2001) IMF and a top-heavy IMF with a power-law exponent of  $-2$  between  $0.5$  and  $300 M_{\odot}$ . The initial gas phase abundance was matched to the stellar metallicity and the metals depleted using the “ISM\_CloudyClassic.dpl” table. The gas-to-dust mass ratio were adjusted similar to Pereira-Santaella et al. (2017). We varied the gas volume density,  $n_H$ , between  $10^2$  and  $10^4 \text{ cm}^{-3}$  in 1 dex steps and the ionization parameters between  $\log U = -6.75$  and  $-1.0$  in 0.25 dex steps. The models are stopped when the temperature drops below  $1000 \text{ K}$  or the  $\text{H}^+$  abundance is below  $0.1\%$ .

In order to trace the temporal evolution of the line ratios, we need to define how  $\log U$  varies with the age of the stellar population.  $\log U$  is proportional to the rate of ionizing photons,  $Q(\text{H})$ . Thus, similar to Rigby & Rieke (2004), we defined, for every combination of IMF and stellar metallicity,  $\log U_0$  as the ionization parameter when  $Q(\text{H})$  is maximum ( $Q(\text{H})_0$ ; typically at ages of  $\sim 1-2 \text{ Myr}$ ), and scaled  $\log U_{\text{age}}$  relative to  $\log U_0$  using the ratio  $Q(\text{H})(\text{age})/Q(\text{H})_0$ . Then, the line emission at each stellar age is interpolated from the grid using  $\log U_{\text{age}}$ .

Figure D.1 shows the  $[\text{Mg IV}]/\text{Hu-12}$  ratio as function of the stellar age for  $\log U_0$  between  $-1.0$  and  $-3.0$ . Only the  $n_H = 10^2 \text{ cm}^{-3}$  ratios are presented since the variation of this ratio in the explored  $n_H$  range ( $10^2-10^4 \text{ cm}^{-3}$ ) is small,  $<30\%$ .

#### D.2. AGN photoionization models

Similar to the star-formation models (Sect. D.1), we assumed a constant density slab. For the incident radiation, we used the three SEDs derived by Jin et al. (2012) for low, medium,

and high Eddington ratios. These SEDs represent a more realistic characterization of the SED of AGN than a power-law (e.g., Ferland et al. 2020). We considered three gas phase abundances ( $0.4 Z_{\odot}$ ,  $Z_{\odot}$ , and  $2 Z_{\odot}$ ) which were depleted using the “ISM\_CloudyClassic.dpl” table and their gas-to-dust mass ratio were adjusted (see Sect. D.1). We varied  $n_H$  between  $10^2$  and  $10^5 \text{ cm}^{-3}$  in 0.5 dex steps and  $\log U$  between  $-4.0$  and  $-1.75$  in 0.25 dex steps. Line ratios derived from these grids are shown in the left panel of Fig. 6.

#### D.3. Shock models

We used MAPPINGS V code version 5.2.0 to create a grid of shock models Sutherland & Dopita (2017). This grid includes several improvements compared to the models presented by Allen et al. (2008). For instance, the fully time-dependent solution for the photoionized precursor is computed for the first time (see Sutherland & Dopita 2017 for details).

The effect of dust is not taken into account by the MAPPINGS V shock code. This is justified for the high-temperature post-shock gas where dust grains can be effectively destroyed (see Allen et al. 2008). However, dust will be present in the photoionized precursor. This is particularly important since Mg is known to condense on silicate grains (e.g., Rogantini et al. 2020). As a first order correction, we reduced the gas phase abundances of metals in the precursor using the default CLOUDY depletion factors (0.2 for Mg). We also updated the atomic parameters relevant for the emission lines of interest (e.g.,  $[\text{Mg IV}]$  and  $[\text{Ar VI}]$ ) to match those used in CLOUDY version 23.01. We used atomic data from the CHIANTI database version 10 (Del Zanna et al. 2021) and the Stout database from CLOUDY (Lykins et al. 2015).

We followed Sutherland & Dopita (2017) to create the grids varying four input parameters: the gas metallicity,  $Z_{\text{gas}}$ ; the shock velocity,  $v_s$ ; the ram pressure parameter,  $R = (n_H/1 \text{ cm}^{-3}) \times (v_s/\text{km s}^{-1})^2$ ; and the magnetic to ram pressure ratio,  $\eta_M = B^2/(4\pi\rho v_s^2)$ , where  $B$  is the magnetic field and  $\rho$  the density. For  $Z_{\text{gas}}$ , we used  $0.5 Z_{\odot}$ ,  $Z_{\odot}$ , and  $2 Z_{\odot}$  and for  $v_s$  we used a logarithmic grid between  $80$  and  $500 \text{ km s}^{-1}$  with  $\sim 0.04$  dex steps. We used three pressures,  $R = 10^4$ ,  $10^6$ , and  $10^8$ , which are equivalent to densities of  $n_H = 1$ ,  $100$ , and  $10^4 \text{ cm}^{-3}$  at  $100 \text{ km s}^{-1}$ . For the magnetic field, we used  $\eta_M = 10^{-4}$ ,  $10^{-2}$ , and  $10^{-1}$ , which correspond to

the “standard”, “moderate”, and “strong” magnetic cases identified in Sutherland & Dopita (2017) and are equivalent to  $B = 5.4$ , 54, and  $170 \mu\text{G}$  for  $R = 10^6$ . The standard magnetic case is presented in the right panel of Fig. 6 and the moderate and strong in Fig. D.2. The main effect of the magnetic field on the [Mg iv]/Hu-12 ratios is that a higher  $v_s$  is needed to obtain the same ratio because more energy is needed to compress the gas when the magnetic field is stronger.

#### D.4. [Mg iv] luminosity from SNe

We estimated the expected [Mg iv] luminosity produced by SNe shocks for a constant star-formation rate, traced by H recombination lines, by combining the shock models and the stellar population evolution models from the BPASS library.

Assuming Case B conditions, the H recombination lines can be used to measure  $Q(\text{H})$ . For temperatures between 5 000 and 10 000 K, the  $\text{H}\alpha/\text{H}\beta$  ratio is 1250–1820 (Storey & Hummer 1995) and  $Q(\text{H})(\text{s}^{-1}) = (0.85 - 1.41) \times 10^{15} L(\text{H}\beta)(\text{erg s}^{-1})$ .

According to the BPASS stellar population models, for metallicities between  $0.4 Z_\odot$  and  $2 Z_\odot$ , and assuming a constant star-formation rate,  $\log(Q(\text{H})(\text{s}^{-1})/\dot{E}_{\text{SN}}(\text{erg s}^{-1})) = 11.72 - 12.10$ , where  $\dot{E}_{\text{SN}}$  is the power released by SNe. This ratio is sensitive to the assumed energy released per SN event ( $10^{51}$  erg), and also to the IMF (e.g., Zapartas et al. 2017). For this calculation, we used the Kroupa (2001) IMF and a top-heavy IMF (see Sect. D.1).

For these metallicities, shock models (Sect. D.3) predict that [Mg iv] is emitted more efficiently at  $v_s \sim 110 - 160 \text{ km s}^{-1}$ . These  $v_s$  are also comparable to the observed dispersion of the [Mg iv] line profiles. Therefore, in this  $v_s$  range,  $\log L([\text{Mg iv}])/\dot{E}_{\text{shock}}$ , where  $\dot{E}_{\text{shock}} = 0.5\rho v_s^3$  is the rate of mechanical energy flux across the shock, is between  $-4.25$  and  $-4.05$  (Fig. D.3). We note that this fraction is very small compared to the  $\sim 0.2\%$  shock energy that is released by some [Fe ii] transitions (e.g., Mouri et al. 2000).

Combining these three relations, matching the abundances of the stellar population and the shock models, and taking into account the Hu-12 emission from the shock (right panel of Fig. 6), the predicted  $\log L([\text{Mg iv}])/L(\text{Hu-12})$  ratio in a region with constant star-formation rate and shocks produced by SNe would be  $-1.4$  and  $-0.5$ .

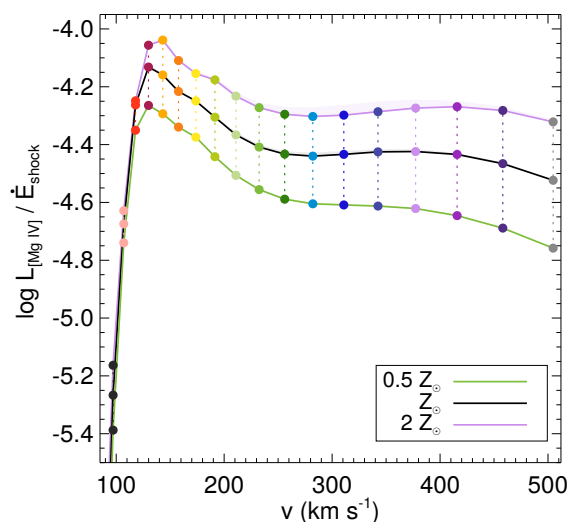


**Fig. D.3.** Ratio between the [Mg iv] luminosity and the rate of mechanical energy flux across the shock,  $\dot{E}_{\text{shock}}$ . The symbols are as in the right panel of Fig. 6.